Controlling electron projectile coherence effects using twisted electrons

A. L. Harris*
Department of Physics, Illinois State University, Normal, Illinois 61790, USA

(Received 5 July 2023; accepted 15 November 2023; published 12 December 2023)

In traditional scattering theory, the incident projectile is assumed to have an infinite coherence length. However, over the last decade, experimental and theoretical studies of collisions using heavy ion projectiles have shown that this assumption is not always valid. This has led to a growing number of studies that specifically examine the effects of the projectile's coherence length on collision cross sections. These studies have used heavy ion projectiles because they offer a straightforward method to control the projectile's coherence length through its momentum, and using these techniques, it has been demonstrated that the projectile's coherence length alters the cross sections. In contrast, it is widely presumed that the coherence length of an electron projectile is always sufficiently large that any effects on the cross sections can be safely neglected. We show that, contrary to this prevailing opinion, coherence effects are observable for electron projectiles and they can be controlled. We calculate triple differential cross sections (TDCSs) for ionization of H_2^+ using twisted electron projectiles in the form of Laguerre-Gauss and Bessel electrons. Effects of the projectile's coherence length are observed through the presence or absence of two-slit interference features in the TDCSs. When the electron projectile's coherence length is large, ionization occurs from either nuclear center of the molecule, and two-slit interference features are visible in the TDCSs. In contrast, when the projectile's coherence length is small, ionization occurs from only one nuclear center and the TDCSs resemble those for ionization of atomic hydrogen. We demonstrate that the intrinsic parameters of the vortex projectiles, such as beam waist and opening angle, can be used to control the coherence length of electron projectiles.

DOI: 10.1103/PhysRevA.108.062810

I. INTRODUCTION

Since the early days of quantum mechanics, charged particle collisions have been a valuable tool to probe the electronic structure of atoms and molecules and elucidate few-body Coulomb interactions. The back-and-forth comparison between experimental measurements and theoretical models has led to sufficiently good agreement that our understanding of many charged particle collisions with simple targets was considered complete [1–6]. However, about a decade ago, measurements of ionization of helium by heavy ion projectiles exposed unexpected discrepancies between established theories and state of the art measurements [7]. In the years since the experiments of [7], a variety of explanations for these discrepancies have been proposed, including, for example, experimental resolution [8], inaccurate theoretical treatment of the projectile-target interaction [9–12], and screening of the target nucleus by inactive electrons [13]. The current leading explanation in the literature is that the projectile's transverse coherence length, a feature typically assumed to be infinite in most quantum mechanical scattering theories, is in fact finite and must be considered when comparing theoretical results with experimental data [14–23]. Several works have demonstrated control of projectile coherence length [14–20,23–31] through experimental design. In particular, projectiles with small coherence length, and particularly those whose coherence length is similar in size or smaller than the target width, can lead to significant alterations of the collision cross sections [15,17]. These effects went unnoticed for many decades because agreement between experiment and theory was generally quite good (e.g., [32,33]) for total and single differential cross sections at small perturbation parameters (ratio of projectile charge to speed) [7,8,34–37]. However, as the availability of fully differential cross section measurements expanded, it opened the door to more rigorous test of theory [7,32,34,38–42], revealing gaps in our understanding and insights into the possible role of projectile coherence length.

To date, most studies of projectile coherence length have used heavy ion projectiles due to their small de Broglie wavelength, and thus small transverse coherence length. In these cases, the transverse coherence length was directly manipulated by changing the projectile's momentum through either the energy or ion type (i.e., mass) [14–17,24], allowing for the effects of the coherence length on collision cross sections to be observed. For electron projectiles, controlling the coherence length through the momentum is more difficult because of their small mass. Even at large velocities, the electron's wavelength remains large, which leads to a coherence length that is typically greater than the target width, preventing coherence effects from appearing in the cross sections. Experimentally, the transverse coherence length is given by $\Delta r = L\lambda/2a$, where a is the width of the collimating slit, L is the distance from the slit to the target, and λ is the de Broglie wavelength [15]. Thus the coherence length is proportional to the de Broglie wavelength, but because L/a is on the order of 100 or greater, the coherence length is much larger than

*alharri@ilstu.edu

the de Broglie wavelength. For example, a proton with a velocity of 1 a.u. has a de Broglie wavelength of 0.003 a.u., while an electron with the same velocity has a wavelength of 6.3 a.u. Even for a 10 keV electron projectile, which is at the higher end of energies typically used in atomic and molecular collisions, the de Broglie wavelength is 0.23 a.u., which yields a transverse coherence length larger than the typical target dimensions of a few atomic units.

Here, we demonstrate a means to study and control the transverse coherence length of electron projectiles on a scale where its effects are clearly observable. We calculate triple differential cross sections (TDCSs) for ionization of H_2^+ using electron vortex projectiles (also called twisted electrons). We show that the intrinsic parameters of the vortex projectiles, such as beam waist and opening angle, can be used to control the coherence length and localization of the impinging projectile at the atomic scale, regardless of the de Broglie wavelength. The projectile is determined to be coherent or incoherent relative to the size of the target molecule by the presence or absence of interference features in the TDCSs.

In the H_2^+ molecule, the target electron density is localized around two nuclear centers. When the incident projectile wave packet is wide enough to perturb the target wave function at both centers (i.e., coherent), the ionization amplitudes from the two centers can interfere. This yields an interference pattern in the TDCS in analogy with the Young's double slit interference experiment using light [43–47]. Thus the TDCSs are expected to show signs of interference effects when the projectile's transverse coherence length is equal to, or larger than, the internuclear separation.

If the incident projectile is incoherent, its transverse coherence length is small, and it is only able to perturb the wave packet localized around one of the nuclear centers. In this case, the TDCS will resemble that of ionization from a single hydrogen atom and no interference features will be observed. Therefore, the shape of the TDCSs is expected to reveal the coherent nature of the incident projectile wave packet relative to the size of the target molecule.

To date, most work with electron vortex projectiles in atomic and molecular collisions has focused on atomic targets [22,48–59] using Bessel and Airy electron beams and is exclusively theoretical. These studies were motivated by the experimental demonstration of these types of electron beams [60–63] and they have predicted that the use of electron vortex projectiles will significantly alter the collision cross sections relative to their nonvortex counterparts [22,48–59]. Recently, a few studies have been undertaken on molecular targets, which showed that like atomic targets, the TDCSs for ionization by a vortex projectile were altered compared to TDCSs with plane wave projectiles [64–66]. For ionization of H_2, it was demonstrated that the incident vortex projectile's orbital angular momentum changed the interference pattern observed in the TDCSs [64].

Despite the many investigations of the role of electron vortex properties on collision cross sections, the idea of using vortex projectiles to study projectile coherence effects has only arisen in the last year [67]. The initial study of such effects was performed on an atomic target, where the observation of coherence effects is challenging. The use of a molecular target to study electron projectile coherence effects is ideal because the presence or absence of interference effects in the TDCSs is dependent upon on the projectile's coherence length. Thus the ionization of molecular targets by electron vortex projectiles provides a straightforward way to directly examine the role of electron projectile coherence. Experimental measurements of projectile coherence effects on interference features in the cross sections require electron vortex projectiles with coherence lengths on the scale of the target, and as demonstrated in [68], the technology to produce such beams exists, making these types of collision experiments possible. The results presented here predict that the coherent nature of electron vortex projectiles can be controlled through their intrinsic properties and that their coherence has a significant and observable effect on the TDCSs.

The remainder of the paper is organized as follows. Section II contains details of the theoretical treatment. Section III presents the TDCSs for LG and Bessel projectiles. Section IV contains a summary and discussion of the work.

II. THEORY

The TDCSs for electron vortex ionization of H_2^+ were calculated using the perturbative first Born approximation (FBA) [48,49], which is applicable for high incident projectile energies of a few hundred eV and small momentum transfer values [69,70]. Here, we use a 1 keV incident projectile with a scattering angle of 1° and an ionized electron energy of 100 eV, yielding a momentum transfer of 0.6 a.u., which makes the FBA applicable and sufficient to capture the relevant features of the TDCS. In the FBA, the TDCS is proportional to the square of the transition matrix T_{fi}^V,

$$\frac{\mathrm{d}^3\sigma}{d\Omega_1 \mathrm{d}\Omega_2 dE_2} = \mu_{pt}^2 \mu_{ie} \frac{k_f k_e}{k_i} \left|T_{fi}^V\right|^2, \tag{1}$$

where

$$T_{fi}^V = -(2\pi)^{3/2} \left\langle \Psi_f \middle| V_i \middle| \Psi_i^V \right\rangle. \tag{2}$$

The reduced mass of the final state ion and ionized electron is μ_{ie} and the reduced mass of the projectile and target molecule is μ_{pt}. The momenta are given by $\vec{k}_i$ for the incident projectile, $\vec{k}_f$ for the scattered projectile, and $\vec{k}_e$ for the ionized electron. Inserting complete sets of position states allows Eq. (2) to be written as an integral over all of position space for each of the particles in the collision. The projectile wave functions are expressed in cylindrical coordinates (ρ_1, φ_1, z_1) and the bound and ionized electron wave functions are expressed in spherical coordinates $(r_2, \theta_2, \varphi_2)$. The origin is located at the target center of mass. Within this geometry, the projectile momenta can be written in terms of their respective longitudinal and transverse components as $\vec{k}_i = k_{i\perp}\hat{\rho}_{1i} + k_{iz}\hat{z}_1$ and $\vec{k}_f = k_{f\perp}\hat{\rho}_{1f} + k_{fz}\hat{z}_1$. We consider here the coplanar scattering geometry, in which the incident projectile, final projectile, and ionized electron momenta all lie in the same plane [x-z plane of Fig. 1(a)].

The initial state wave function is expressed as a product of the incident vortex wave function $\chi_{\vec{k}_i}^V(\vec{r}_1)$ and the target molecular wave function $\Phi(\vec{r}_2, \vec{R})$,

$$\Psi_i^V = \chi_{\vec{k}_i}^V(\vec{r}_1)\Phi(\vec{r}_2, \vec{R}) \tag{3}$$

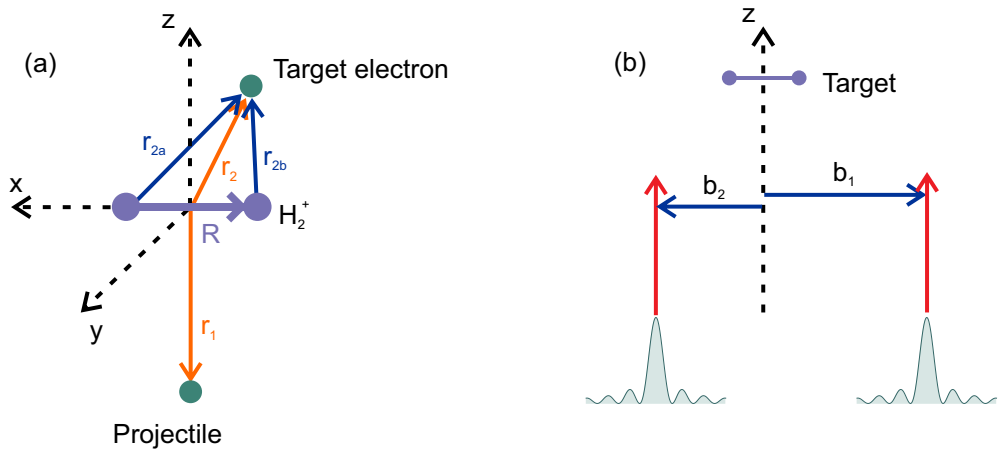

FIG. 1. (a) Coordinate system for $e^- + H_2^+$ collision system. The incident projectile propagates along the z direction and the target molecule is shown with an alignment perpendicular to the incident projectile beam. The orange vectors represent the position of the projectile ($\vec{r}_1$) and target electron ($\vec{r}_2$) relative to the center of mass of the target. The blue vectors represent the position of the target electron relative to each nuclear center ($\vec{r}_{2a}$, $\vec{r}_{2b}$). (b) Schematic of incident projectile wave packet impinging on a target atom. The shaded green region is the transverse profile of an incident Bessel projectile. Because the LG and Bessel twisted wave functions are not uniform in the transverse direction, an impact parameter $\vec{b}$ must be defined. Two possible values of $\vec{b}$ are shown ($\vec{b}_1$, $\vec{b}_2$), and the red arrows indicate the incident projectile's propagation direction.

where $\vec{R}$ is the internuclear vector [see Fig. 1(a)]. The incident projectile vortex beam is chosen to be either a localized Laguerre-Gauss beam or a delocalized Bessel beam. Because the Bessel and LG vortex beams are nonuniform in the transverse direction, their transverse alignment relative to the target center of mass must be considered. The alignment of the projectile's transverse center with the target's center of mass is accounted for through the introduction of an impact parameter $\vec{b}$, such that $\vec{b}$ points transversely from the target center of mass to the center of the impinging vortex projectile wave packet [Fig. 1(b)].

For $\vec{b} = 0$, the wave function for the Bessel projectile is given by

$$\chi^V_{\vec{k}_i}(\vec{r}_1, \vec{b} = 0) = \chi^B_{\vec{k}_i,l}(\vec{r}_1, \vec{b} = 0) = \frac{e^{il\varphi_1}}{2\pi} J_l(k_{i\perp}\rho_1) e^{ik_{iz}z_1}, \quad (4)$$

where $J_l(k_{i\perp}\rho_1)$ is the Bessel function and $k_{i\perp}$ is the incident transverse momentum that can be written in terms of the opening angle α:

$$k_{\perp i} = k_i \sin\alpha. \quad (5)$$

Using a superposition of tilted plane waves [51], the Bessel wave function can be written as

$$\chi^B_{\vec{k}_i,l}(\vec{r}_1, \vec{b} = 0) = \frac{(-i)^l}{(2\pi)^2} \int_0^{2\pi} d\phi_{ki} e^{il\phi_{ki}} e^{i\vec{k}_i\cdot\vec{r}_1}. \quad (6)$$

Similarly, for $\vec{b} = 0$, the wave function for the LG projectile is given by [51]

$$\chi^V_{\vec{k}_i}(\vec{r}_1, \vec{b} = 0) = \chi^{\mathrm{LG}}_{\vec{k}_i,l}(\vec{r}_1, \vec{b} = 0)$$
$$= \frac{N}{w_0} e^{il\varphi_1} \left(\frac{\rho_1\sqrt{2}}{w_0}\right)^{|l|} L_n^{|l|}\left(\frac{2\rho_1^2}{w_0^2}\right) e^{-2\rho_1^2/w_0^2} \frac{e^{ik_{iz}z_1}}{\sqrt{2\pi}}, \quad (7)$$

where N is a normalization constant,[1] w_0 is the beam waist, and $L_n^{|l|}(\frac{2\rho_1^2}{w_0^2})$ is an associated Laguerre polynomial with orbital angular momentum l about the z axis and index n that is related to the number of nodes for a given l. For ease of computation, it is convenient to use the expression of the LG wave function as a convolution of Bessel functions over transverse momentum [51]:

$$\chi^{\mathrm{LG}}_{\vec{k}_i,l}(\vec{r}_1, \vec{b}=0) = \frac{N}{\sqrt{2}} \frac{e^{il\varphi_1}}{n!} \int_0^\infty dk_{i\perp}\, e^{-w_0^2 k_{i\perp}^2/8} \left(\frac{w_0 k_{i\perp}}{\sqrt{8}}\right)^{2n+l+1}$$
$$\times J_l(k_{i\perp}\rho_1) \frac{e^{ik_{iz}z_1}}{\sqrt{2\pi}}. \quad (8)$$

Combining Eqs. (8) and (4), the LG wave function can be expressed as a convolution of Bessel projectile wave functions over transverse momentum:

$$\chi^{\mathrm{LG}}_{\vec{k}_i,l}(\vec{r}_1, \vec{b} = 0) = \frac{N\sqrt{\pi}}{n!} \int_0^\infty dk_{i\perp} e^{-\frac{k_{i\perp}^2 w_0^2}{8}} \left(\frac{k_{i\perp} w_0}{\sqrt{8}}\right)^{2n+l+1}$$
$$\times \chi^B_{\vec{k}_i,l}(\vec{r}_1, \vec{b} = 0). \quad (9)$$

Physically, Eqs. (8) and (9) imply that, unlike the Bessel projectile, the LG projectile has no well-defined transverse momentum. When the beam waist w_0 is large, the factor $e^{-\frac{k_{i\perp}^2 w_0^2}{8}} (\frac{k_{i\perp} w_0}{\sqrt{8}})^{2n+l+1}$ in the integral is more localized at small transverse momentum values, resulting in the convolution favoring a few Bessel wave functions with small transverse momenta (i.e., those with small α). These are the Bessel wave functions that are most similar to the plane wave function, causing the LG projectile to be delocalized in space with a large coherence length. When the beam waist is small, this

[1]The expression for N in [51] is slightly incorrect. N was calculated numerically to ensure normalization of the LG wave function.

same factor in Eqs. (8) and (9) is a broader function of transverse momentum centered at larger transverse momentum values, resulting in many Bessel wave functions contributing to the convolution. In this case, the LG wave function is localized in space, but delocalized in momentum.

The initial state H_2^+ molecular wave function is written as a linear combination of atomic orbitals with each orbital having an effective nuclear charge of Z_{eff} [71]:

$$\Phi(\vec{r}_2) = \frac{Z_{\text{eff}}^{\frac{3}{2}}}{\sqrt{2}}[e^{-Z_{\text{eff}}|\vec{r}_{2a}|} + e^{-Z_{\text{eff}}|\vec{r}_{2b}|}]. \tag{10}$$

The coordinates $\vec{r}_{2a}$ and $\vec{r}_{2b}$ are the position vectors for the target electron relative to each of the nuclei [see Fig. 1(a)]:

$$\vec{r}_{2a} = \vec{r}_2 + \vec{R}/2,$$
$$\vec{r}_{2b} = \vec{r}_2 - \vec{R}/2. \tag{11}$$

For an equilibrium separation of $|\vec{R}| = 2$ a.u., $Z_{\text{eff}} = 1.25$ yields the correct ionization potential of 29.9 eV.

The final state wave function is written as a product of the scattered projectile wave function $\chi_{\vec{k}_f}(\vec{r}_1)$, the ionized electron wave function $\chi_{\vec{k}_e}(\vec{r}_2)$, and the postcollision Coulomb interaction (PCI) M_{ee}:

$$\Psi_f = \chi_{\vec{k}_f}(\vec{r}_1)\chi_{\vec{k}_e}(\vec{r}_2)M_{ee}. \tag{12}$$

Given the large projectile energy, it is sufficient to assume that the scattered projectile leaves the collision as a plane wave given by

$$\chi_{\vec{k}_f}(\vec{r}_1) = \frac{e^{i\vec{k}_f\cdot\vec{r}_1}}{(2\pi)^{3/2}}. \tag{13}$$

This scattered projectile plane wave has no well-defined orbital angular momentum, but rather contains contributions from all possible orbital angular momenta. Thus the incident vortex projectile's well-defined, quantized orbital angular momentum is partially or totally transferred to the target-ionized electron system during the collision [48,53,72]. Likewise, orbital angular momentum can be transferred from the target to the projectile during the collision. Both of these processes lead to the scattered projectile having no well-defined orbital angular momentum and its description as a plane wave.

A two-center Coulomb wave [73] is used to model the ionized electron,

$$\chi_{\vec{k}_e}(\vec{r}_2) = \frac{e^{i\vec{k}_e\cdot\vec{r}_2}}{(2\pi)^{\frac{3}{2}}}\Gamma(1-i\eta)e^{-\frac{\pi\eta}{2}}{}_1F_1(i\eta, 1, -ik_e r_{2a} - i\vec{k}_e\cdot\vec{r}_{2a})$$
$$\times\,\Gamma(1-i\eta)e^{-\frac{\pi\eta}{2}}{}_1F_1(i\eta, 1, -ik_e r_{2b} - i\vec{k}_e\cdot\vec{r}_{2b}), \tag{14}$$

where $\Gamma(1-i\eta)$ is the gamma function and $\eta = Z_C Z_e/k_e$ is the Sommerfeld parameter with Z_C the effective, screened nuclear charge seen by the ionized electron and $Z_e = 1$ is the charge of the electron. In the calculations presented here, we use $Z_C = 1$, which is the charge of each of the protons in the final state. The ejected electron wave function of Eq. (14) is orthogonalized to the target electron wave function of Eq. (10) through the Gram-Schmidt procedure.

The Ward-Macek factor [74] is used to include the postcollision Coulomb repulsion between the two outgoing final state electrons,

$$M_{ee} = N_{ee}\left|{}_1F_1\left(\frac{i}{2k_{fe}}, 1, -2ik_{fe}r_{\text{ave}}\right)\right|, \tag{15}$$

where

$$N_{ee} = \sqrt{\frac{\pi}{k_{fe}\left(e^{\frac{\pi}{k_{fe}}} - 1\right)}}. \tag{16}$$

The relative momentum is $k_{fe} = \frac{1}{2}|\vec{k}_f - \vec{k}_e|$ and the average coordinate $r_{\text{ave}} = \frac{\pi^2}{16\epsilon}\left(1 + \frac{0.627}{\pi}\sqrt{\epsilon}\ln\epsilon\right)^2$, where $\epsilon = (k_f^2 + k_e^2)/2$ is the total energy of the two outgoing electrons.

The perturbation V_i is the Coulomb interaction between the projectile and target molecule, which is given by

$$V_i = \frac{-1}{|\vec{r}_1 - \vec{R}/2|} + \frac{-1}{|\vec{r}_1 + \vec{R}/2|} + \frac{1}{r_{12}}. \tag{17}$$

Combining the above equations allows for the transition matrices for on-center Bessel and LG projectiles to be written in terms of the transition matrix for a nonvortex incident plane wave projectile T_{fi}^{NV}:

$$T_l^B(\vec{b} = 0) = \frac{(-i)^l}{2\pi}\int_0^{2\pi} d\phi_{k_i} e^{il\phi_{k_i}} T_{fi}^{NV} \tag{18}$$

and

$$T_{l,n}^{\text{LG}}(\vec{b} = 0) = \frac{N\sqrt{\pi}}{n!}\int_0^\infty d\kappa\; e^{-\frac{w_0^2\kappa^2}{8}}\left(\frac{w\kappa}{\sqrt{8}}\right)^{2n+l+1} T_l^B. \tag{19}$$

In a scattering experiment with a gas target, a specific impact parameter cannot be selected or controlled, and it is therefore necessary for theory to integrate over all possible impact parameters in order to provide an accurate comparison with possible experiments. For a Bessel projectile, the TDCS integrated over impact parameter is given by [48,55]

$$\left.\frac{d^3\sigma_B}{d\Omega_1 d\Omega_2 dE_2}\right|_{\text{int } b} = \mu_{pt}^2\mu_{ie}\frac{k_f k_e}{k_{iz}(2\pi)}\int_0^{2\pi}\left|T_{fi}^{NV}\right|^2 d\phi_{k_i}, \tag{20}$$

and for a LG projectile, the TDCS integrated over impact parameter is given by [67]

$$\left.\frac{d^3\sigma_{LG}}{d\Omega_1 d\Omega_2 dE_2}\right|_{\text{int } b} = \mu_{pt}^2\mu_{ie}\frac{k_f k_e}{k_i}\frac{N^2\pi}{(n!)^2(2\pi)}\int_0^\infty \frac{e^{-\frac{k_{i\perp}^2 w_0^2}{4}}}{k_{i\perp}^2}$$
$$\times\left(\frac{k_{i\perp}^2 w_0^2}{8}\right)^{2n+l+1}\left|T_{fi}^{NV}\right|^2 k_{i\perp}dk_{i\perp}d\phi_{k_i}. \tag{21}$$

For the Bessel projectile, the average over impact parameter is analogous to a sum over orbital angular momentum [51] and thus the effects of the projectile's quantized orbital angular momentum are washed out in the TDCSs. For a LG projectile, the average over impact parameter has a similar effect except that the projectile's orbital angular momentum still appears in the weighting factor of the integral over the projectile's transverse momentum and effects associated with a specific orbital angular momentum may still appear in the TDCSs.

TABLE I. Transverse coherence length δ of LG projectiles in atomic units calculated using Eq. (22). The LG parameters n and l are labeled as (n, l). For (1,0) LG projectiles, δ is listed for the case when all peaks are included in the density, as well as for when only the primary peak is included.

	δ all peaks (0,0)	δ all peaks (1,0)	δ primary peak (1,0)	δ all peaks (0,1)
$w_0 = 0.5$ a.u.	0.24	0.32	0.15	0.24
$w_0 = 1$ a.u.	0.46	0.46	0.30	0.48
$w_0 = 4$ a.u.	1.86	2.52	1.24	1.94
$w_0 = 8$ a.u.	3.70	5.04	2.48	3.86

III. RESULTS

A. Controlling transverse coherence length using Laguerre-Gauss projectiles

The LG and Bessel projectiles provide different means through which to examine the role of projectile coherence and localization. For LG projectiles, the transverse coherence length δ can be defined using the quantum mechanical uncertainty $\Delta\rho$ of the transverse wave packet,

$$\delta = 2\Delta\rho = [\langle\rho^2\rangle - \langle\rho\rangle^2]^{1/2}, \tag{22}$$

which varies linearly with the beam waist $\Delta\ \rho \propto w_0$. The factor of 2 is included to account for the presence of projectile density on both sides of the origin (i.e., when the azimuthal angle is 0 or π). The projectile's transverse coherence length can be directly controlled through the beam waist. In addition, the transverse coherence length changes with the Laguerre-Gauss indices n and l [from now on labeled as (n, l)]. A few sample values of the transverse coherence length for LG projectiles are listed in Table I and the projectile transverse densities are plotted in Fig. 2. For comparison, the internuclear separation for H_2^+ is 2 a.u., and it is expected that interference features will be present in the TDCSs when $\delta \gtrsim 2$ a.u. A 1 keV electron, as is used here, has a de Broglie wavelength of 0.73 a.u., which results in an experimental transverse coherence length much larger than the internuclear separation. For (1,0) LG projectiles, the transverse density contains more than one peak, and Table I includes the coherence length calculated for all peaks [i.e., the integral over ρ in Eq. (22) runs from 0 to ∞], as well as for only the primary (largest) peak [i.e., the integral over ρ in Eq. (22) runs from 0 to the first zero in the transverse density]. For (0,1) LG projectiles, the transverse density has a node at the origin, whose radius increases with increasing beam waist. The coherence length defined in Eq. (22) accounts for both the width of the peak and radius of the node.

Figure 3 shows the coplanar TDCSs for ionization of H_2^+ by 1 keV LG projectiles for different l and n as a function of ejected electron angle and beam waist. The projectile is scattered at a fixed angle of 1° and the ionized electron energy is 100 eV. The TDCSs have been averaged over impact parameter. The color indicates the magnitude of the TDCS (cooler colors are smaller TDCSs and warmer colors are larger TDCSs). Two fixed orientations of the H_2^+ molecule are shown relative to the incident beam direction. The first column shows TDCSs for H_2^+ aligned parallel to the beam direction and the second column shows TDCSs when the molecule is aligned perpendicular to the beam direction. The third column shows

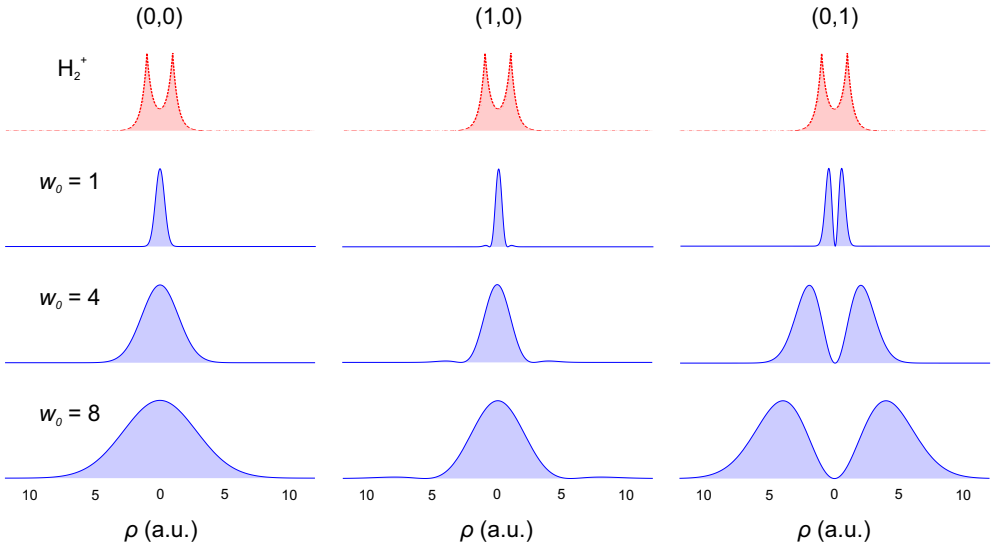

FIG. 2. Transverse profiles of the H_2^+ electron density (top row, red dashed line) and the LG beam (rows 2–4, blue solid line) as a function of transverse distance ρ. The LG parameters n and l are labeled at the top for each column (n, l) and the beam waist is labeled at the left for each row (w_0). All profiles are normalized to 1 to provide a qualitative comparison of width. The target H_2^+ electron density is the same for each column.

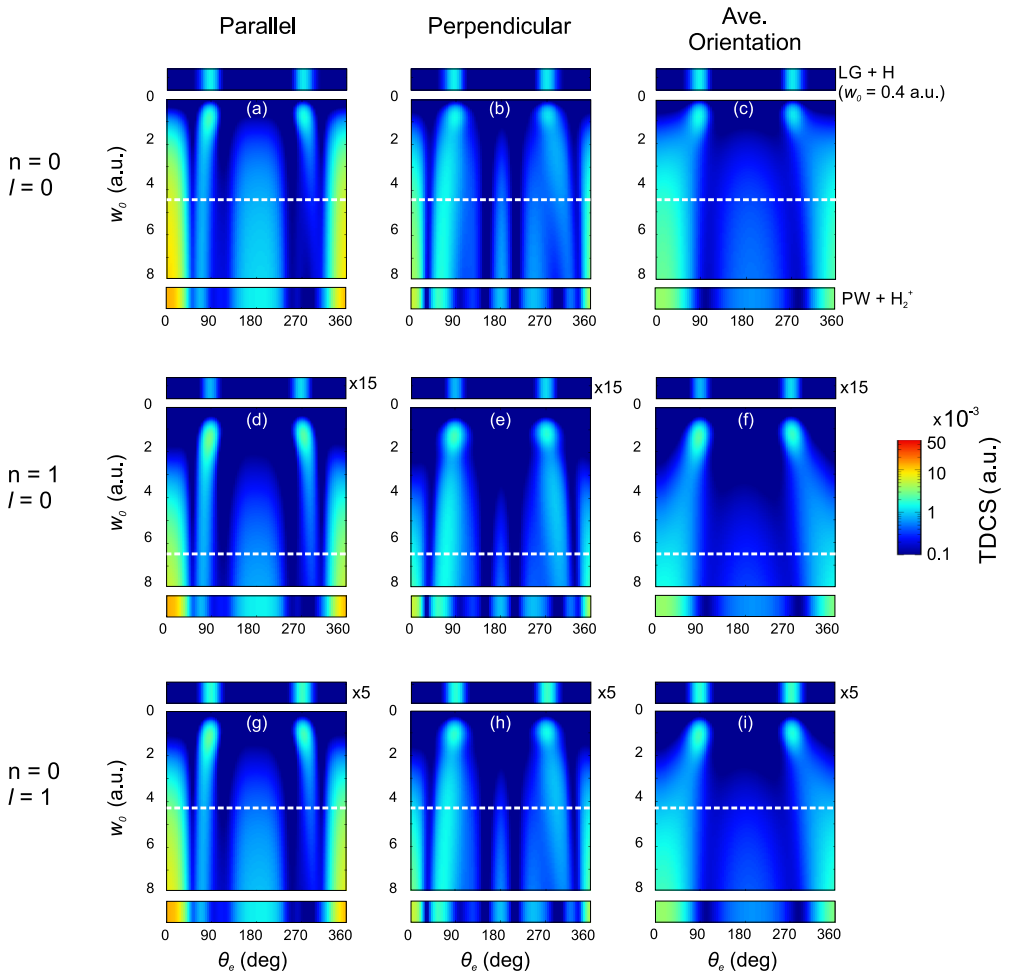

FIG. 3. TDCSs for ionization of H_2^+ by 1 keV LG projectiles as a function of beam waist (w_0) on the vertical axis and ejected electron angle (θ_e) on the horizontal axis. The projectile scattering angle was 1° and the ionized electron energy was 100 eV. The magnitude of the TDCS is indicated by color. Panels (a)–(c) show TDCSs for $n = 0$, $l = 0$ (0,0); (d)–(f) for $n = 1$, $l = 0$ (1,0); (g)–(i) for $n = 0$, $l = 1$ (0,1). In the first column, the molecule's axis is aligned parallel with the incident beam direction. In the second column, the molecule's axis is aligned perpendicular to the incident beam direction. In the third column, the TDCSs were averaged over all molecular axis orientations. The horizontal dashed white line indicates the beam waist value that yields a transverse coherence length of $\delta = 2$ a.u. (i.e., equal to the internuclear separation). Within each panel, the top row is the TDCS for ionization of atomic hydrogen by a LG projectile with $w_0 = 0.4$ a.u. [as indicated in (c)]. The atomic hydrogen TDCSs have been multiplied by 15 (d)–(f) and 5 (g)–(i). The bottom row is the TDCS for ionization of H_2^+ by a plane wave [as indicated in (c)].

the TDCSs averaged over all possible orientations. The white horizontal dashed line represents the beam waist value that yields a transverse coherence length of $\delta = 2$ a.u. (i.e., equal to the internuclear separation).

The bottom row of each panel in Fig. 3 is a color bar that contains the TDCS for ionization of H_2^+ by a plane wave projectile [see label in Fig. 3(c)]. In this case, the projectile is completely delocalized and the TDCSs show clear interference features due to ionization from the two nuclear centers. The top row of each panel in Fig. 3 shows a color bar that contains the TDCS for ionization of atomic H by a LG projectile with $w_0 = 0.4$ a.u. [see label in Fig. 3(c)]. In this case, the projectile is localized, and no interference effects are present due to the single ionization center of the atomic target.

For ionization of H_2^+ by a LG projectile with a small beam waist, the TDCSs show two narrow peaks at $\theta_e = 90°$ and 270°, independent of molecular orientation. The shape of these TDCSs is similar to the TDCS for ionization of H by a narrow LG projectile (color bar above each panel), which confirms that projectiles with small transverse coherence length cause ionization from only one of the nuclear centers.

As the beam waist increases, these two peaks shift slightly toward the forward direction, and an additional peak at $\theta_e = 0°$ appears. As the beam waist is further increased, a peak at $\theta_e = 180°$ appears and the TDCSs then show the same interference structures as the TDCS for a plane wave projectile. The presence of the full pattern of interference structures in the LG TDCSs occurs approximately at a beam waist value that corresponds to a projectile transverse coherence length equal to the internuclear separation. This indicates that when the transverse coherence length is greater than or equal to the internuclear separation, ionization can occur from either nuclear center with the amplitudes interfering. The value of the beam waist that results in a transverse coherence length equal to the internuclear separation can be interpreted as a threshold value for the coherence of the electron projectile.

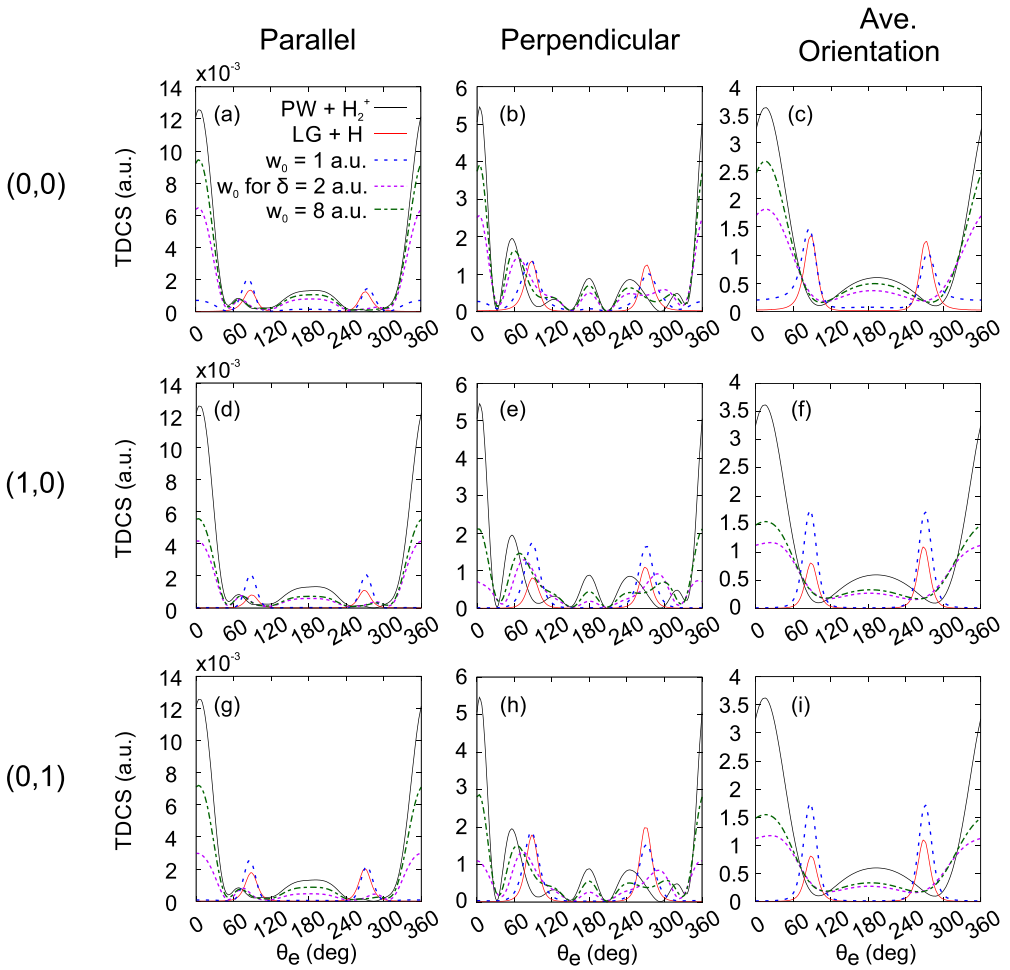

FIG. 4. TDCSs for ionization of H_2^+ by 1 keV LG projectiles as a function of ejected electron angle (θ_e) for select values of beam waist w_0. The kinematics is identical to that in Fig. 3. Panels (a)–(c) show TDCSs for $n = 0$, $l = 0$ (0,0); (d)–(f) for $n = 1$, $l = 0$ (1,0); (g)–(i) for $n = 0$, $l = 1$ (0,1). In the first column, the molecule's axis is aligned parallel with the incident beam direction. In the second column, the molecule's axis is aligned perpendicular to the incident beam direction. In the third column, the TDCSs were averaged over all molecular axis orientations. The short dashed pink line shows the cross section for a value of w_0 that corresponds to a transverse coherence length of $\delta = 2$ a.u. This value is $w_0 = 4.5$ a.u. for (a)–(c), $w_0 = 6.5$ a.u. for (d)–(f), and $w_0 = 4.2$ a.u. for (g)–(i).

Beyond the threshold value, the interference structures persist in the TDCSs with very little change which is consistent with the requirement that the transverse coherence length must be large enough to perturb the target electron wave function at both nuclear centers in order for the ionization amplitudes to interfere.

The detailed interference structures in the TDCSs are more readily observed in Fig. 4, which contains the TDCSs for a few select values of w_0. For $w_0 = 1$ a.u., it is clear that only two peak structures exist in the TDCS, much like those for ionization from a single hydrogen atom. However, when the transverse coherence length is greater than the internuclear separation, the TDCSs show multiple peak structures similar to the TDCS for ionization of H_2^+ by a plane wave. In particular, well-defined peaks at $\theta_e \approx 0^\circ$ and 180° are present for coherent projectiles, which are features that distinguish the TDCSs for coherent projectiles from those of incoherent projectiles.

In Fig. 3, the onset of interference features in the TDCSs for (1,0) LG projectiles approximately coincides with the beam waist threshold found for the coherence length of the primary peak and not all peaks, indicating that the small side peak for the (1,0) LG projectile does not significantly influence the TDCSs and that ionization primarily occurs due to the main peak. As shown in Table I and Fig. 2, for a given beam waist, the transverse coherence length of the LG beam for (0,0) is larger than that of the primary lobe of a LG beam with (1,0), and this results in the interference effects being observed at a smaller beam waist value for (0,0) LG projectiles [Figs. 3(a)–3(c)] than for (1,0) LG projectiles [Figs. 3(d)–3(f)].

For (0,1) LG projectiles [Figs. 3(g)–3(i)], the LG transverse profile contains two equal lobes with a node at the origin. The width of this node increases with increasing beam waist, and its presence is caused by the nonzero orbital angular momentum of the (0,1) LG projectile. The TDCSs for (0,1) LG projectiles are very similar to those of (0,0) LG projectiles, and the threshold beam waist value that leads to a coherent projectile is also similar. This indicates that for the kinematics considered here, the orbital angular momentum of the projectile plays a small role. Additionally, the double peaked structure of the projectile's transverse density for (0,1)

LG projectiles does not alter the TDCSs compared to those of the (0,0) LG projectile. This is likely due to the uncertainty in the alignment of the projectile and target for the TDCSs presented in Fig. 3 (i.e., the average of the TDCSs over impact parameter). The inclusion of TDCSs for projectiles with nonzero impact parameters introduces contributions to the TDCSs from additional orbital angular momenta [55] and has the effect of washing out orbital angular momentum–specific features in the TDCSs.

Some minor qualitative differences are observed in the TDCSs for large beam waist ($w_0 = 8$ a.u.) relative to the plane wave TDCSs. These are most noticeable when the molecular axis is perpendicular to the beam direction, in which case more individual peaks are observed in the plane wave TDCSs than the LG TDCSs (Figs. 3 and 4). These differences are due to the localization of the LG projectile, despite the large beam waist. When the beam waist was increased to $w_0 \geqslant 20$ a.u. (not shown), the TDCSs were identical to the plane wave TDCSs.

The TDCSs averaged over molecular orientation show fewer interference features because any orientation-dependent effects are averaged out. However, the delineation in the shape of the TDCSs for coherent and incoherent projectiles is still observable. At small beam waist, the TDCSs exhibit only the two peaks at 90° and 270° that are characteristic of ionization from a single nuclear center. As the beam waist increases, these peaks broaden and become a single forward peak centered at 0°. This shift and broadening occurs at a smaller beam waist value for the (0,0) LG projectile and at a larger beam waist value for the (0,1) and (1,0) LG projectiles, consistent with the dependence of the transverse coherence length on beam waist for the different LG parameters. For beam waists larger than the threshold for a coherent projectile, a peak is observed at 180° in the TDCSs as a result of interference from two nuclear centers.

B. Controlling localization with Bessel projectiles

For the Bessel projectile, the transverse coherence as defined in Eq. (22) is infinite, but an effective width (or transverse localization) of the wave packet can be defined. As the projectile opening angle increases, the transverse momentum increases and the individual peaks in the projectile transverse density become narrower (see Fig. 5). For $l > 0$, there is a node in the transverse density whose width increases as the opening angle decreases. In the limit that $\alpha = 0$ and $l = 0$, the Bessel projectile is identical to a completely delocalized plane wave. Thus the opening angle provides a mechanism by which to change the effective transverse localization of the Bessel projectile. To quantify the localization, we assume that the dominant contribution to ionization comes from the primary (largest) peak of the Bessel wave function, and we define the transverse localization of the Bessel projectile as the transverse uncertainty calculated with Eq. (22) using only the density up to the first zero (i.e., the integral over ρ runs from 0 to the first zero in the transverse density). A similar assumption led to accurate predictions of coherence length for the (1,0) LG projectile. A few values of the transverse localization for the Bessel projectile are listed in Table II for the two lowest orbital angular momentum values, which are expected to be the predominant influence on the TDCSs, as described below.

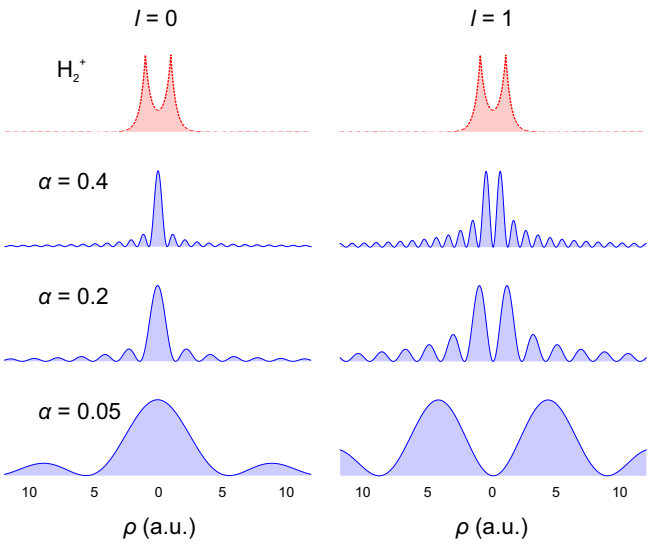

FIG. 5. Transverse profiles of the H_2^+ electron density (top row, red dashed line) and the Bessel beam (rows 2–4, blue solid line) as a function of transverse distance ρ. The Bessel projectile orbital angular momentum is labeled at the top for each column (l) and the opening angle is labeled at the left for each row (α). All profiles are normalized to 1 to provide a qualitative comparison of width. The target H_2^+ electron density is the same for each column.

Figure 6 shows the coplanar TDCSs for ionization of H_2^+ by a Bessel projectile as a function of ejected electron angle and opening angle. As in Fig. 3, the color indicates magnitude of the TDCS, and two fixed orientations of the H_2^+ molecule are shown in addition to the TDCSs averaged over all possible orientations. The TDCSs have been averaged over impact parameter, which results in contributions from all orbital angular momenta of the projectile contributing to the TDCS [55]. Thus, for Bessel projectiles averaged over impact parameter, a specific orbital angular momentum of the projectile cannot be identified, although prior work on the ionization of atomic targets has shown that the dominant contributions to the TDCSs are from low orbital angular momentum terms of the projectile [48,64]. This averaging implies that no features of the TDCSs can be attributed to the transverse profiles of the Bessel projectiles with specific orbital angular momentum. However, as Table II shows, the transverse localization increases as the opening angle decreases for all values of l, and thus it can be correlated with features observed in the TDCSs.

TABLE II. Transverse localization δ of Bessel projectiles in atomic units for projectiles with orbital angular momenta of $l = 0, 1$.

	δ primary peak $l = 0$	δ primary peak $l = 1$
$\alpha = 0.4$ rad	0.28	0.38
$\alpha = 0.2$ rad	0.56	0.76
$\alpha = 0.1$ rad	1.10	1.50
$\alpha = 0.05$ rad	2.20	3.00

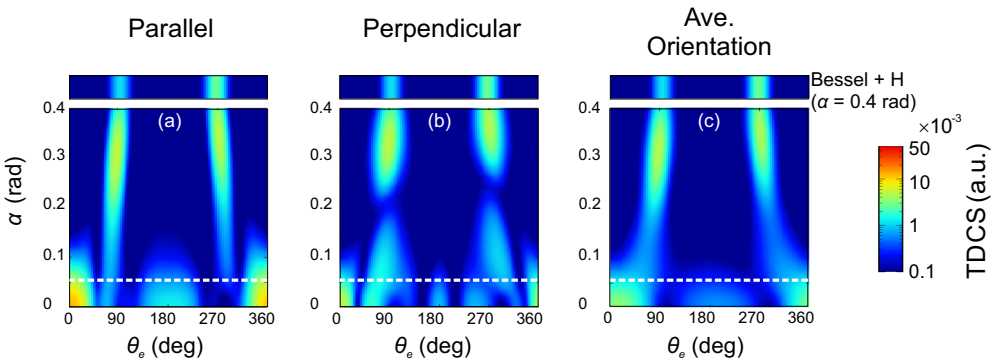

FIG. 6. TDCSs for ionization of H_2^+ by 1 keV Bessel projectiles as a function of opening angle (α) on the vertical axis and ejected electron angle (θ_e) on the horizontal axis. The projectile scattering angle was 1° and the ionized electron energy was 100 eV. The magnitude of the TDCS is indicated by color. Panel (a) shows the TDCS for the molecule's axis aligned parallel with the incident beam direction. Panel (b) shows the TDCS for the molecule's axis aligned perpendicular to the incident beam direction. In panel (c), the TDCSs were averaged over all molecular axis orientations. The horizontal dashed white line indicates the opening angle value that yields a transverse localization of $\delta =$ 2 a.u. (i.e., equal to the internuclear separation). Within each panel, the top row is the TDCS for ionization of atomic hydrogen by a Bessel projectile with $\alpha = 0.4$ rad [as indicated in (c)]. A trace along the x axis for $\alpha = 0$ yields the TDCS for ionization of H_2^+ by plane wave.

The top row of each panel in Fig. 6 is a color bar that contains the TDCS for ionization of atomic hydrogen by a Bessel projectile with $\alpha = 0.4$ rad [see label in Fig. 6(c)]. In this case, the projectile is localized, and no interference effects are present due to the single ionization center of the atomic target. A trace along the horizontal axis of each panel ($\alpha = 0$) yields the plane wave TDCS in which the projectile is completely delocalized. Here, clear interference features are visible due to ionization from the two nuclear centers.

As shown in Fig. 5 and Table II, Bessel projectiles with large opening angles have a highly localized main peak in their transverse profile and a small transverse localization. At large opening angles, the TDCSs for ionization of H_2^+ resemble those of ionization of atomic hydrogen by a localized projectile, independent of molecular orientation. This demonstrates that Bessel projectiles with large opening angles behave as localized wave packets and are only able to cause ionization from one of the nuclear centers.

As the opening angle decreases, the Bessel projectile's transverse density broadens and becomes less localized. Much like with LG projectiles, the peaks in the TDCSs shift toward the forward direction as the projectile transverse density broadens, and below a threshold value of opening angle, interference structures are observed in the TDCSs. The horizontal white dashed lines in Fig. 6 show the opening angle that yields a transverse localization of the $l = 0$ Bessel projectile of 2 a.u. Figure 6 shows that for opening angles less than this threshold value, the projectile's transverse profile is broad enough to cause ionization from both nuclear centers, resulting in an interference pattern consistent with ionization from two nuclear centers. Because the threshold value of the opening angle yields a Bessel projectile transverse localization that coincides with the internuclear separation of the target, we can conclude that despite the Bessel projectile's infinite transverse coherence length, it behaves as a localized wave packet. Additionally, the threshold value of the opening angle calculated using only the main peak of the $l = 0$ projectile density qualitatively agrees with the appearance of the interference features in the TDCSs. This is an indication that ionization predominantly occurs due to the main peak in the projectile density and supports our use of only this peak to estimate projectile coherence. It also indicates that the lowest orbital angular momentum value is the dominant contribution to the TDCSs, even though contributions from all angular momenta are included.

Figure 7 shows the TDCSs or a select few values of α. For large opening angles, the TDCSs clearly resemble the TDCSs for atomic hydrogen, exhibiting only two peak structures at $\theta_e \approx 90°$ and 270°. For opening angles less than or equal to the threshold value, the TDCSs more closely resemble those of a plane wave projectile with peaks at $\theta_e \approx 0°$ and 180°. These similarities indicate that for small opening angles, the projectile behaves coherently with the TDCSs exhibiting two-center interference features.

Overall, the TDCSs for LG and Bessel projectiles exhibit qualitatively similar behavior as either the beam waist or opening angle is changed. At small beam waist and large opening angle, the TDCSs resemble those for ionization of atomic hydrogen, indicating a highly localized and incoherent projectile. In contrast, at large beam waist and small opening angle, the TDCSs resemble those for ionization of H_2^+ by a plane wave projectile, indicating a coherent projectile. Thus projectile coherence can be controlled for both LG and Bessel projectiles through the choice of the wave packet parameters, regardless of de Broglie wavelength.

IV. SUMMARY

In the last decade, much attention has been focused on the role of projectile coherence and localization in heavy particle atomic and molecular collisions, and it has been shown that theoretical models must consider the transverse coherence length of the projectile when calculating collision cross sections. However, until recently, no studies have examined the role of projectile coherence in electron-impact collisions because the de Broglie wavelength, and the corresponding transverse coherence length, of a plane wave electron projectile were sufficiently large to ensure that the projectile

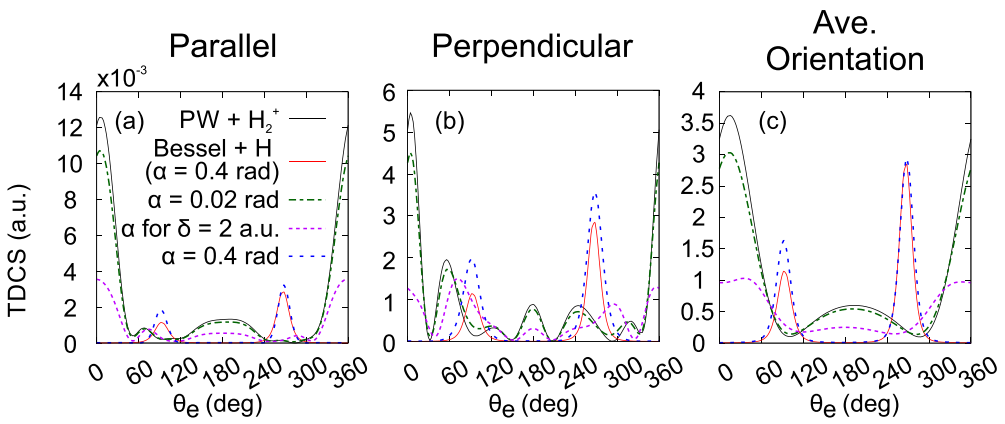

FIG. 7. TDCSs for ionization of H_2^+ by 1 keV Bessel projectiles as a function of ejected electron angle (θ_e) for select opening angles α. The kinematics is the same as in Fig. 6. Panel (a) shows the TDCS for the molecule's axis aligned parallel with the incident beam direction. Panel (b) shows the TDCS for the molecule's axis aligned perpendicular to the incident beam direction. In panel (c), the TDCSs were averaged over all molecular axis orientations. The short dashed pink line shows the cross section for a value of $\alpha = 0.05$ rad that corresponds to a transverse coherence length of $\delta = 2$ a.u.

was fully coherent. We have demonstrated that it is possible to alter an electron projectile's coherence by using vortex projectiles and that the projectile's transverse coherence length has a significant and observable effect on the collision cross sections.

We presented theoretical TDCSs for electron-impact ionization of H_2^+ using Laguerre-Gauss and Bessel projectiles. We controlled the projectile's transverse coherence length and localization through the parameters of the vortex projectile, such as beam waist and opening angle. The use of a projectile with a small beam waist or large opening angle yielded TDCSs that resembled those found for ionization of atomic hydrogen, indicating that the projectile was localized and that ionization occurred from only one of the nuclear centers of the molecule. In contrast, a projectile with a large beam waist or small opening angle yielded TDCSs that resembled those found for nonvortex, plane wave projectiles, and showed an interference pattern indicative of ionization from both nuclear centers.

We identified threshold values of beam waist and opening angle that separated coherent, delocalized projectiles from incoherent, localized projectiles. These threshold values coincided with the calculated coherence length and localization that equaled the molecule's internuclear separation, consistent with the premise that interference features in the TDCSs are observable when the projectile's transverse coherence length is greater than or equal to the internuclear separation. The presence and or absence of interference features in the TDCSs provided a clear indicator of projectile coherence, and our results demonstrated that the coherence of an electron projectile can be controlled and studied using twisted wave packets.

The results presented here for the simplest of molecules, H_2^+, can easily be extended to more complex targets, such as larger molecules or surfaces. Because the ionization cross sections for vortex projectiles are written in terms of their plane wave nonvortex counterparts, any previously developed techniques for the study of molecular ionization with more complex targets can easily be implemented into this framework. Additionally, it is possible, with some approximation, to extend the vortex cross sections to more sophisticated perturbative models, such as the Coulomb distorted wave (CDW) or distorted wave Born approximation (DWBA) models. While the derivation was not rigorous, prior work was performed in which the plane wave TDCS that appears in the vortex cross section expression was replaced with a DWBA TDCS, and physically reasonable results were achieved [75]. Naturally, the validity of any of these models can only be tested through comparison with experiment, which currently does not exist, as far as we know. Additionally, the use of nonperturbative models to study electron vortex collisions presents a much greater challenge and to date has not been achieved, to the best of our knowledge.

In the last decade and a half, advances in both experimental production of electron vortex projectiles and theoretical predictions of their properties, interactions with matter, and uses have been rapid. This work provides evidence of the ability to control electron coherence through a vortex projectile's properties and that the effects of coherence will be experimentally observable. Such control is anticipated to open the door to further applications in which the wave and coherence properties of electrons are used to probe atomic scale structures.

ACKNOWLEDGMENT

We gratefully acknowledge the support of the National Science Foundation under Grant No. PHY-1912093.

[1] T. N. Rescigno, M. Baertschy, W. A. Isaacs, and C. W. McCurdy, Collisional breakup in a quantum system of three charged particles, Science **286**, 2474 (1999).

[2] I. Bray, Close-coupling approach to Coulomb three-body problems, Phys. Rev. Lett. **89**, 273201 (2002).

[3] J. Colgan and M. S. Pindzola, Double- and triple-differential cross sections for the low-energy electron-impact

ionization of hydrogen, Phys. Rev. A **74**, 012713 (2006).
[4] K. Bartschat and I. Bray, *S*-wave model for electron-hydrogen scattering, Phys. Rev. A **54**, R1002 (1996).
[5] K. Bartschat, I. Bray, D. V. Fursa, and A. T. Stelbovics, Absolute triple-differential cross sections for ionization-excitation of helium, Phys. Rev. A **76**, 024703 (2007).
[6] K. Bartschat, I. Bray, D. V. Fursa, and A. T. Stelbovics, Erratum: Absolute triple-differential cross sections for ionization-excitation of helium [Phys. Rev. A **76**, 024703 (2007)]; Phys. Rev. A **77**, 029903(E) (2008).
[7] M. Schulz, R. Moshammer, D. Fischer, H. Kollmus, D. H. Madison, S. Jones, and J. Ullrich, Three-dimensional imaging of atomic four-body processes, Nature (London) **422**, 48 (2003).
[8] J. Fiol, S. Otranto, and R. E. Olson, Critical comparison between theory and experiment for C^{6+}+He fully differential ionization cross sections, J. Phys. B: At., Mol. Opt. Phys. **39**, L285 (2006).
[9] M. Schulz, M. Dürr, B. Najjari, R. Moshammer, and J. Ullrich, Reconciliation of measured fully differential single ionization data with the first Born approximation convoluted with elastic scattering, Phys. Rev. A **76**, 032712 (2007).
[10] R. E. Olson and J. Fiol, Dynamics underlying fully differential cross sections for fast C^{6+}+He collisions, J. Phys. B: At., Mol. Opt. Phys. **36**, L365 (2003).
[11] J. Colgan, M. S. Pindzola, F. Robicheaux, and M. F. Ciappina, Fully differential cross sections for the single ionization of He by C^{6+} ions, J. Phys. B: At., Mol. Opt. Phys. **44**, 175205 (2011).
[12] F. Járai-Szabó and L. Nagy, Semiclassical description of kinematically complete experiments, J. Phys. B: At., Mol. Opt. Phys. **40**, 4259 (2007).
[13] M. Foster, J. L. Peacher, M. Schulz, D. H. Madison, Z. Chen, and H. R. J. Walters, Unexpected higher-order effects in charged particle impact ionization at high energies, Phys. Rev. Lett. **97**, 093202 (2006).
[14] K. N. Egodapitiya, S. Sharma, A. Hasan, A. C. Laforge, D. H. Madison, R. Moshammer, and M. Schulz, Manipulating atomic fragmentation processes by controlling the projectile coherence, Phys. Rev. Lett. **106**, 153202 (2011).
[15] S. Sharma, A. Hasan, K. N. Egodapitiya, T. P. Arthanayaka, G. Sakhelashvili, and M. Schulz, Projectile coherence effects in electron capture by protons colliding with H_2 and He, Phys. Rev. A **86**, 022706 (2012).
[16] K. Schneider, M. Schulz, X. Wang, A. Kelkar, M. Grieser, C. Krantz, J. Ullrich, R. Moshammer, and D. Fischer, Role of projectile coherence in close heavy ion-atom collisions, Phys. Rev. Lett. **110**, 113201 (2013).
[17] S. Sharma, T. P. Arthanayaka, A. Hasan, B. R. Lamichhane, J. Remolina, A. Smith, and M. Schulz, Fully differential study of interference effects in the ionization of H_2 by proton impact, Phys. Rev. A **90**, 052710 (2014).
[18] F. Járai-Szabó and L. Nagy, Theoretical investigations on the projectile coherence effects in fully differential ionization cross sections, Eur. Phys. J. D **69**, 4 (2015).
[19] L. Sarkadi, I. Fabre, F. Navarrete, and R. O. Barrachina, Loss of wave-packet coherence in ion-atom collisions, Phys. Rev. A **93**, 032702 (2016).
[20] F. Navarrete, M. F. Ciappina, L. Sarkadi, and R. O. Barrachina, The role of the wave packet coherence on the ionization cross section of He by p^+ and C^{6+} projectiles, Nucl. Instrum. Methods Phys. Res., Sect. B **408**, 165 (2017).
[21] K. A. Kouzakov, Theoretical analysis of the projectile and target coherence in COLTRIMS experiments on atomic ionization by fast ions, Eur. Phys. J. D **71**, 63 (2017).
[22] D. V. Karlovets, G. L. Kotkin, and V. G. Serbo, Scattering of wave packets on atoms in the Born approximation, Phys. Rev. A **92**, 052703 (2015).
[23] X. Wang, K. Schneider, A. LaForge, A. Kelkar, M. Grieser, R. Moshammer, J. Ullrich, M. Schulz, and D. Fischer, Projectile coherence effects in single ionization of helium, J. Phys. B: At., Mol. Opt. Phys. **45**, 211001 (2012).
[24] M. Schulz, A. Hasan, B. Lamichhane, T. Arthanayaka, M. Dhital, S. Bastola, L. Nagy, S. Borbély, and F. Járai-Szabó, Projectile coherence effects in simple atomic systems, J. Phys.: Conf. Ser. **1412**, 062007 (2020).
[25] L. Gulyás, S. Egri, and A. Igarashi, Theoretical investigation of the fully differential cross sections for single ionization of He in collisions with 75-keV protons, Phys. Rev. A **99**, 032704 (2019).
[26] F. Navarrete, M. F. Ciappina, and R. O. Barrachina, Coherence properties of the projectile's beam: The missing piece of the C^{6++} He ionization puzzle, J. Phys.: Conf. Ser. **1412**, 152033 (2020).
[27] R. O. Barrachina, F. Navarrete, and M. F. Ciappina, Atomic concealment due to loss of coherence of the incident beam of projectiles in collision processes, Atoms **9**, 5 (2021).
[28] T. Voss, B. R. Lamichhane, M. Dhital, R. Lomsadze, and M. Schulz, Differential study of projectile coherence effects on double capture processes in p^+ Ar collisions, Atoms **8**, 10 (2020).
[29] F. Navarrete, R. Barrachina, and M. F. Ciappina, Distortion of the ionization cross section of He by the coherence properties of a C^{6+} beam, Atoms **7**, 31 (2019).
[30] L. Nagy, F. Járai-Szabó, S. Borbély, and K. Tőkési, Projectile coherence effects analyzed using impact parameters determined by classical trajectory Monte Carlo calculations, J. Phys.: Conf. Ser. **1412**, 152032 (2020).
[31] S. Bastola, M. Dhital, S. Majumdar, A. Hasan, R. Lomsadze, J. Davis, B. Lamichhane, S. Borbély, L. Nagy, and M. Schulz, Interference effects in fully differential ionization cross sections near the velocity matching in p + He collisions, Atoms **10**, 119 (2022).
[32] H. Gassert, O. Chuluunbaatar, M. Waitz, F. Trinter, H-K. Kim, T. Bauer, A. Laucke, Ch. Müller, J. Voigtsberger, M. Weller, J. Rist, M. Pitzer, S. Zeller, T. Jahnke, L. Ph. H. Schmidt, J. B. Williams, S. A. Zaytsev, A. A. Bulychev, K. A. Kouzakov, H. Schmidt-Böcking *et al.*, Agreement of experiment and theory on the single ionization of helium by fast proton impact, Phys. Rev. Lett. **116**, 073201 (2016).
[33] R. Moshammer, P. D. Fainstein, M. Schulz, W. Schmitt, H. Kollmus, R. Mann, S. Hagmann, and J. Ullrich, Initial state dependence of low-energy electron emission in fast ion atom collisions, Phys. Rev. Lett. **83**, 4721 (1999).
[34] N. V. Maydanyuk, A. Hasan, M. Foster, B. Tooke, E. Nanni, D. H. Madison, and M. Schulz, Projectile–residual-target-ion scattering after single ionization of helium by slow proton impact, Phys. Rev. Lett. **94**, 243201 (2005).
[35] M. McGovern, C. T. Whelan, and H. R. J. Walters, C^{6+}-impact ionization of helium in the perpendicular plane: Ionization to

the ground state, excitation-ionization, and relativistic effects, Phys. Rev. A **82**, 032702 (2010).

[36] R. T. Pedlow, S. F. C. O'Rourke, and D. S. F. Crothers, Fully differential cross sections for 3.6 MeV u^{-1} Au^{Zp+}+He collisions, Phys. Rev. A **72**, 062719 (2005).

[37] A. B. Voitkiv and B. Najjari, Projectile-target core interaction in single ionization of helium by 100-MeV/u C^{6+} and 1-GeV/u U^{92+} ions, Phys. Rev. A **79**, 022709 (2009).

[38] R. Dörner, V. Mergel, R. Ali, U. Buck, C. L. Cocke, K. Froschauer, O. Jagutzki, S. Lencinas, W. E. Meyerhof, S. Nüttgens, R. E. Olson, H. Schmidt-Böcking, L. Spielberger, K. Tökesi, J. Ullrich, M. Unverzagt, and W. Wu, Electron-electron interaction in projectile ionization investigated by high resolution recoil ion momentum spectroscopy, Phys. Rev. Lett. **72**, 3166 (1994).

[39] D. H. Madison, D. Fischer, M. Foster, M. Schulz, R. Moshammer, S. Jones, and J. Ullrich, Probing scattering wave functions close to the nucleus, Phys. Rev. Lett. **91**, 253201 (2003).

[40] M. Schulz, R. Moshammer, A. N. Perumal, and J. Ullrich, Triply differential single-ionization cross sections in fast ion-atom collisions at large perturbation, J. Phys. B: At., Mol. Opt. Phys. **35**, L161 (2002).

[41] D. Fischer, R. Moshammer, M. Schulz, A. Voitkiv, and J. Ullrich, Fully differential cross sections for the single ionization of helium by ion impact, J. Phys. B: At., Mol. Opt. Phys. **36**, 3555 (2003).

[42] R. Moshammer, M. Unverzagt, W. Schmitt, J. Ullrich, and H. Schmidt-Böcking, A 4π recoil-ion electron momentum analyzer: A high-resolution "microscope" for the investigation of the dynamics of atomic, molecular and nuclear reactions, Nucl. Instrum. Methods Phys. Res., Sect. B **108**, 425 (1996).

[43] N. Stolterfoht, B. Sulik, V. Hoffmann, B. Skogvall, J. Y. Chesnel, J. Rangama, F. Frémont, D. Hennecart, A. Cassimi, X. Husson, A. L. Landers, J. A. Tanis, M. E. Galassi, and R. D. Rivarola, Evidence for interference effects in electron emission from H_2 colliding with 60 MeV/u Kr^{34+} ions, Phys. Rev. Lett. **87**, 023201 (2001).

[44] D. Misra, U. Kadhane, Y. P. Singh, L. C. Tribedi, P. D. Fainstein, and P. Richard, Interference effect in electron emission in heavy ion collisions with H_2 detected by comparison with the measured electron spectrum from atomic hydrogen, Phys. Rev. Lett. **92**, 153201 (2004).

[45] S. Chatterjee, D. Misra, A. H. Kelkar, L. C. Tribedi, C. R. Stia, O. A. Fojón, and R. D. Rivarola, Young-type interference effect on angular distribution of secondary electrons emitted from H_2 in collisions with fast electrons, Phys. Rev. A **78**, 052701 (2008).

[46] D. S. Milne-Brownlie, M. Foster, J. Gao, B. Lohmann, and D. H. Madison, Young-type interference in $(e, 2e)$ ionization of H_2, Phys. Rev. Lett. **96**, 233201 (2006).

[47] E. M. S. Casagrande, A. Naja, F. Mezdari, A. Lahmam-Bennani, P. Bolognesi, B. Joulakian, O. Chuluunbaatar, O. Al-Hagan, D. H. Madison, D. V. Fursa, and I. Bray, $(e, 2e)$ ionization of helium and the hydrogen molecule: Signature of two-centre interference effects, J. Phys. B: At., Mol. Opt. Phys. **41**, 025204 (2008).

[48] A. L. Harris, A. Plumadore, and Z. Smozhanyk, Ionization of hydrogen by electron vortex beam, J. Phys. B: At., Mol. Opt. Phys. **52**, 094001 (2019); Corrigendum: Ionization of hydrogen by electron vortex beam, **53**, 109501 (2020).

[49] A. Plumadore and A. L. Harris, Projectile transverse momentum controls emission in electron vortex ionization collisions, J. Phys. B: At., Mol. Opt. Phys. **53**, 205205 (2020).

[50] A. Plumadore and A. L. Harris, Electron spectra for twisted electron collisions, J. Phys. B: At., Mol. Opt. Phys. **54**, 235204 (2022).

[51] R. Van Boxem, B. Partoens, and J. Verbeeck, Rutherford scattering of electron vortices, Phys. Rev. A **89**, 032715 (2014).

[52] R. Van Boxem, B. Partoens, and J. Verbeeck, Inelastic electron-vortex-beam scattering, Phys. Rev. A **91**, 032703 (2015).

[53] S. Lloyd, M. Babiker, and J. Yuan, Quantized orbital angular momentum transfer and magnetic dichroism in the interaction of electron vortices with matter, Phys. Rev. Lett. **108**, 074802 (2012).

[54] N. Dhankhar, A. Mandal, and R. Choubisa, Double ionization of helium by twisted electron beam, J. Phys. B: At., Mol. Opt. Phys. **53**, 155203 (2020).

[55] V. Serbo, I. P. Ivanov, S. Fritzsche, D. Seipt, and A. Surzhykov, Scattering of twisted relativistic electrons by atoms, Phys. Rev. A **92**, 012705 (2015).

[56] O. Matula, A. G. Hayrapetyan, V. G. Serbo, A. Surzhykov, and S. Fritzsche, Radiative capture of twisted electrons by bare ions, New J. Phys. **16**, 053024 (2014).

[57] V. P. Kosheleva, V. A. Zaytsev, A. Surzhykov, V. M. Shabaev, and Th. Stöhlker, Elastic scattering of twisted electrons by an atomic target: Going beyond the Born approximation, Phys. Rev. A **98**, 022706 (2018).

[58] C. Lei and G. Dong, Chirality-dependent scattering of an electron vortex beam by a single atom in a magnetic field, Phys. Rev. A **103**, 032815 (2021).

[59] D. Grosman, N. Sheremet, I. Pavlov, and D. Karlovets, Elastic scattering of Airy electron packets on atoms, Phys. Rev. A **107**, 062819 (2023).

[60] M. Uchida and A. Tonomura, Generation of electron beams carrying orbital angular momentum, Nature (London) **464**, 737 (2010).

[61] B. J. McMorran, A. Agrawal, I. M. Anderson, A. A. Herzing, H. J. Lezec, J. J. McClelland, and J. Unguris, Electron vortex beams with high quanta of orbital angular momentum, Science **331**, 192 (2011).

[62] V. Grillo, G. C. Gazzadi, E. Mafakheri, S. Frabboni, E. Karimi, and R. W. Boyd, Holographic generation of highly twisted electron beams, Phys. Rev. Lett. **114**, 034801 (2015).

[63] N. Voloch-Bloch, Y. Lereah, Y. Lilach, A. Gover, and A. Arie, Generation of electron Airy beams, Nature (London) **494**, 331 (2013).

[64] N. Dhankhar and R. Choubisa, Electron impact single ionization of hydrogen molecule by twisted electron beam, J. Phys. B: At., Mol. Opt. Phys. **54**, 015203 (2020).

[65] N. Dhankhar, Neha, and R. Choubisa, Dynamics of twisted electron impact ionization of CH_4 and NH_3 molecule, Atoms **11**, 82 (2023).

[66] N. Dhankhar and R. Choubisa, Triple-differential cross section for the twisted-electron-impact ionization of the water molecule, Phys. Rev. A **105**, 062801 (2022).

[67] A. L. Harris, Projectile coherence effects in twisted electron ionization of helium, Atoms **11**, 79 (2023).

[68] J. Verbeeck, P. Schattschneider, S. Lazar, M. Stöger-Pollach, S. Löffler, A. Steiger-Thirsfeld, and G. Van Tendeloo, Atomic scale electron vortices for nanoresearch, Appl. Phys. Lett. **99**, 203109 (2011).

[69] J. W. Hooper, D. S. Harmer, D. W. Martin, and E. W. McDaniel, Comparison of electron and proton ionization data with the Born approximation predictions, Phys. Rev. **125**, 2000 (1962).

[70] D. Bote and F. Salvat, Calculations of inner-shell ionization by electron impact with the distorted-wave and plane-wave Born approximations, Phys. Rev. A **77**, 042701 (2008).

[71] H. Bräuning, I. Reiser, A. Diehl, A. Theiß, E. Sidky, C. L. Cocke, and E. Salzborn, Charge transfer in collisions of H^{2+} ions with He^{2+} and Ar^{2+}, J. Phys. B: At., Mol. Opt. Phys. **34**, L321 (2001).

[72] S. M. Lloyd, M. Babiker, and J. Yuan, Interaction of electron vortices and optical vortices with matter and processes of orbital angular momentum exchange, Phys. Rev. A **86**, 023816 (2012).

[73] P. F. Weck, O. A. Fojón, B. Joulakian, C. R. Stia, J. Hanssen, and R. D. Rivarola, Two-center continuum approximation with correct boundary conditions for single-electron emission in e^- + H_2 collisions, Phys. Rev. A **66**, 012711 (2002).

[74] S. J. Ward and J. H. Macek, Wave functions for continuum states of charged fragments, Phys. Rev. A **49**, 1049 (1994).

[75] A. L. Harris, Single and double scattering mechanisms in ionization of helium by electron vortex projectiles, J. Phys. B: At., Mol. Opt. Phys. **54**, 155203 (2021).